Hindawi
Shock and Vibration
Volume 2018, Article ID 2917591, 13 pages
https://doi.org/10.1155/2018/2917591

Research Article

Analysis of the Deformation and Damage of Clamped Square Plates under Near-Field Explosion Loads

Jian He,[1] **Xiaoshu Guan**,[1] **Huipin Chen**,[2] **and Xiaodan Sun**[1]

[1]*College of Aerospace and Civil Engineering, Harbin Engineering University, Harbin, China*
[2]*China Railway Construction Engineering Group Co., Ltd., Beijing Branch, Beijing 100160, China*

Correspondence should be addressed to Xiaodan Sun; sunxiaodan@hrbeu.edu.cn

Received 20 April 2018; Revised 6 July 2018; Accepted 16 July 2018; Published 2 September 2018

Academic Editor: Yuri S. Karinski

The deformation and damage mechanism of shell structures under near-field explosion loads has been of great significance in the theoretical study of impact dynamics and may serve as a dependable theoretic basis for the antiexplosion design of shell structures. In this paper, the plastic zone and crevasse size of clamped square plates under near-field explosion loads were discussed based on the plastic hinge law and energy theory. The crevasse size of a plate moving at motion modes I and *II* under medium load was obtained according to the ultimate plastic strain criterion. Furthermore, the plastic zone under a high load was determined in terms of the movement law of a plastic hinge line. When the applied load ended, the crevasse sizes of the plates at motion modes III and IV were deduced on the basis of the principle of energy conservation. Finally, numerical simulation was used to analyse the deformation and damage mechanism of the shell structures under near-field explosion loads. The theory and method proposed in this paper are verified using ANSYS software and compared with the experimental results. This study verifies the validity of the proposed approach for analysis of the deformation and damage of a clamped square plate under near-field explosion loads.

1. Introduction

Shell structures are widely used in naval vessels, aircraft, and tanks due to their special properties, such as simple construction, being light weight, and good bearing capacity [1–4]. However, shell structures are often subjected to explosion loads or shock waves in practical applications [5–7]. It is necessary to investigate the plastic dynamic response, residual deformation, and damage of the thin plate subjected to an explosion load.

Generally, the dynamic response of thin plates under explosion loads depends on the applied load, material properties, and boundary conditions [8–10]. Considerable efforts have been made to investigate the dynamic response of materials under explosion loads. Houlston and Desrochers [11] calculated the dynamic plastic response of a clamped square plate subjected to blast loading by applying the ADINA procedure. Spranghers et al. [12] proposed an inverse method that uses full-field optical measurements taken during the first milliseconds of a free air explosion to identify the plastic response of aluminum plates subjected to sudden blast loads, and the results verify that the proposed methods can be successfully used to analyse the plastic behaviour of metals subjected to blast waves. Breslavsky et al. [13] experimentally and numerically studied the deformation and fracture of impact-loaded thin steel square plates and discussed the numerical-experimental approach for fracture prediction in plates under repetitive impact loading. Zheng et al. [14] investigated the large deflection behaviour of clamped stiffened plates subjected to confined blast loads through experiments, theoretical analysis, and numerical simulations; it was proven that the proposed calculation model is of high precision and practicability by comparing the numerical results. Li et al. [15, 16] studied the blast response of plates with preformed holes under blast loading; furthermore, the author discussed the damage level at places where cracks might form, the dynamic stress concentration coefficient, and stress status change and analysed the influence of preformed holes on the failure mode. Kazanci and Mecitoglu [17] used the virtual work

principle to analyse and discuss the nonlinear dynamic response of a laminated composite plate subjected to blast load, and finite element results in the literature show good agreement with their approximate numerical analysis results. Yao et al. [18] developed a new dimensionless number that takes into account the influence of blast load, strength of material, and structural dimensions for the dynamic response of box-shaped structures subjected to internal blast loading based on the governing equations of a fully clamped plate. However, a theoretical analysis on the deformation and damage of clamped square plates under near-field explosion load is still limited and requires further study.

In this paper, the plastic zone and crevasse size of a clamped square plate with different types of motion modes are discussed under medium and high loads. After theoretical analysis, the deformation and damage of the plate under the action of near-field explosion load are simulated.

The numerical simulation results are in good agreement with the theoretical analysis results, and the parameter correctness of various material models and state equations has been verified. These studies have laid a foundation for the numerical simulation of explosion problems and provide theoretical guidance for practical applications.

2. Model Simplification and Yield Criterion

2.1. Explosion Load Simplification. The explosion load can be simplified to a triangle load with an ascent stage, as shown in Figure 1, and can be defined as follows:

$$p = \begin{cases} \dfrac{p_m}{t_m} t, & 0 \le t \le t_m, \\ \dfrac{p_m}{t_m - t_s}\left(t - t_s\right), & t_m \le t \le t_s, \end{cases} \tag{1}$$

where p_m is the peak pressure of the explosion load, t_m is the time required for the load to reach the peak value, and t_s is the duration of the applied load.

2.2. Yield Criterion. To simplify the calculations, the yield curve in a square shape plate (Figure 2) is used. It is the expansion of the *Tresca* hexagonal yield curve, which can be defined as follows:

$$\begin{aligned} &\max\left(\left|M_1\right|, \left|M_2\right|\right) = M_s \\ &M_1, M_2 = \frac{1}{2}\left(M_x + M_y\right) \pm \frac{1}{2}\left[\left(M_x - M_y\right)^2 + 4M_{xy}^2\right]^{1/2}, \\ &M_s = \sigma_0 h^2. \end{aligned} \tag{2}$$

In (2), h is the half thickness of the plate.

The length and thickness of the clamped square plate are $2l$ and $2h$, respectively. The near-field explosion loads are applied to the square plate uniformly with a value of p. The coordinate system selected is shown in Figure 3, and a new coordinate is proposed defined as follows:

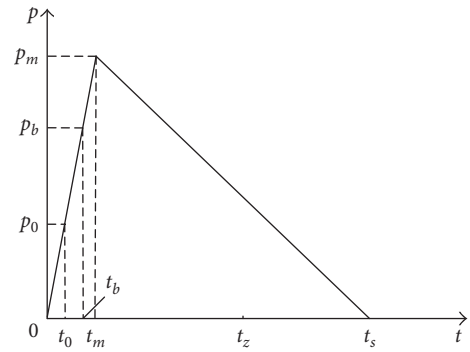

Figure 1: Triangular blast load diagram.

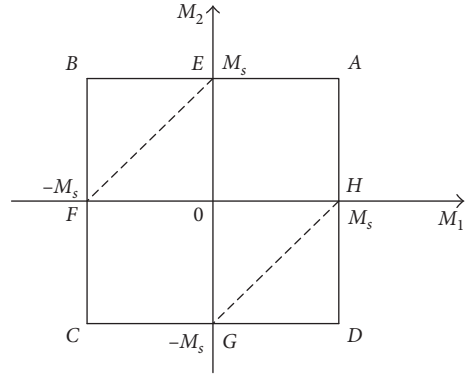

Figure 2: Approximate yield curve of the plate.

$$z = \frac{x + y}{\sqrt{2}l}. \tag{3}$$

The ultimate pressure of the plate subjected to a horizontal, static, uniformly distributed load is $p_0 = 12M_s/l^2$. Under a moderate load of $p_0 < p_m < p_b = 2p_0$, the moving hinge line will not appear in the plate, and the corresponding velocity field is in the form of a tetrahedral pyramid. Under a high load of $p_m > p_b = 2p_0$, the moving hinge line will occur in the plate with a hexahedron velocity field.

Under moderate load, the square plates move in the form of a tetrahedral pyramid. This movement means that when $p_0 < p_m \le p_{mb1}$, at the time of $t = t_0$, the movement of the deformable mechanism with a pyramid begins, the velocity of the plate increases first and then decreases, but it stops before the end of the explosive load. While $p_{mb1} < p_m \le 2p_0$, at the end of the load, the plate will continue to move because the speed of the plate is not zero; under the action of inertia, the velocity gradually drops to zero, and the plate is static.

Under high load, at first, the velocity field is in the form of a tetrahedral pyramid, the moving hinge line appears in the plate when the load suddenly disappears, and the hinge line moves to the centre of the plate; thus, the top platform will gradually shrink until it vanishes.

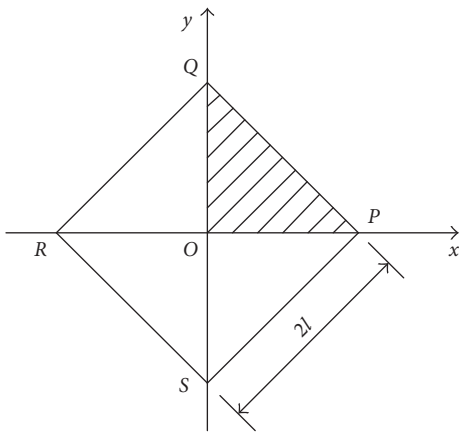

Figure 3: Structural diagram of the plate.

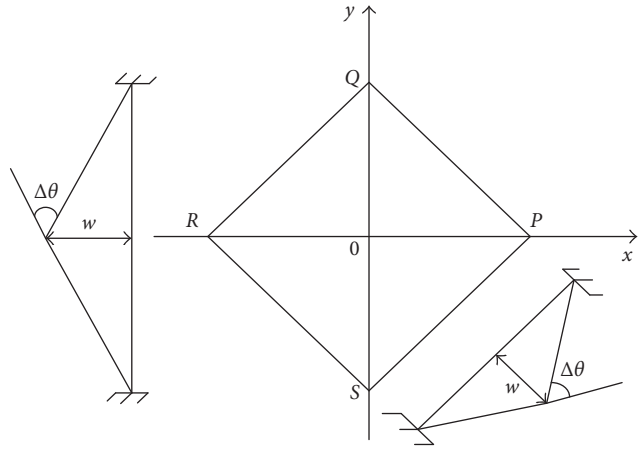

Figure 4: Deformation diagram of the plate.

3. Plastic Deformation and Crevasse Size of the Square Plate under a Medium Load

Under the load of $p_0 < p_m < p_b$, an immobile plastic hinge line appears along the four edges and diagonals of the plate, whereas the remaining area of the plate is rigid. The deformation of the plate is shown in Figure 4.

The square plate cracks first in the middle section, and then, the plastic hinge lines located at the diagonals of the plate continue to crack, finally leaving a cracked hole on the plate. When the plate stops moving, the deflection does not increase, and the cracks do not propagate. Hence, the plastic strain is not greater than the ultimate plastic strain of a point on the plastic hinge line. The point located at the outer edge of the crevasse can further determine the size of the crevasse.

On the plastic hinge line OQ, the stretching effect along the y direction can be ignored because the crevasse occurs in the middle of the plate. As a result, the plastic strain of each point at the plastic hinge line consists of the tensile strain caused by transverse displacement and the flexural strain caused by bending.

Considering a point on OQ with a y distance to origin, the tensile strain ε_{xt} as a result of the transverse displacement can be calculated. The calculated deformation diagram is shown in Figure 5.

As shown in Figure 5, the distance of the selected point with the y distance to the origin point becomes y_1 after the load is applied. Thus,

$$y_1 = l - (l - y)\cos\theta. \tag{4}$$

The transverse tensile strain in the x direction is calculated as follows:

$$\varepsilon_{xt} = \left(\frac{l}{y} - 1\right)(1 - \cos\theta). \tag{5}$$

The calculated diagram of bending strain is shown in Figure 6. The flexural strain of a point at the plastic hinge line is calculated as follows:

$$\varepsilon_{xb} = h\kappa_x, \tag{6}$$

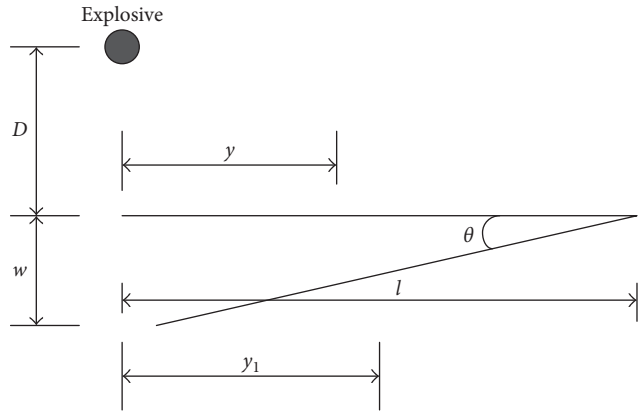

Figure 5: Calculation of plate deformation.

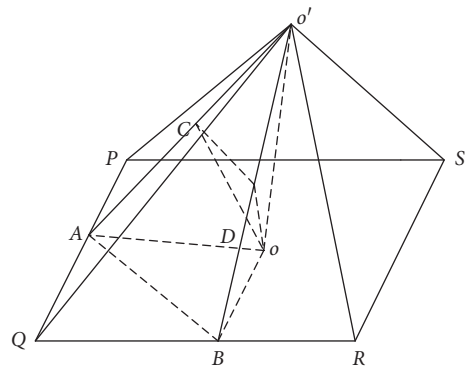

Figure 6: Calculation of the bending strain of the plate.

where κ_x is the bending curvature of OQ and can be defined by the following formula:

$$\kappa_x = \frac{\phi_1}{C}, \tag{7}$$

where ϕ_1 is the relative angle of the plate on both sides of the plastic hinge and C is the width of the bending deformation zone. The value of $4h$ was assigned to C in this paper [19].

Using the Law of Cosines, in ΔOCD,

$$\phi_1 = \arccos\frac{OC^2 + OD^2 - CD^2}{2OC \cdot OD} = \arccos\left(1 + \frac{OO'^2}{l^2}\right)^{-1}. \tag{8}$$

Hence, the bending strain can be expressed as follows:

$$\varepsilon_{xb} = \frac{h}{C}\phi_1 = \frac{1}{4}\arccos\frac{1}{1+\left(OO'^2/l^2\right)}, \tag{9}$$

where OO' is the residual deflection of the plate centre.

According to [11], the deflection of the plate centre point can be expressed as follows:

$$w_1(t) = \frac{2}{\rho_0}\int_{t_0}^{t}(t-\tau)\left[p(\tau) - p_0\right]d\tau. \tag{10}$$

Then, the total plastic strain at this point is the superposition of tensile strain and bending strain:

$$\varepsilon_x = \left(\frac{l}{y} - 1\right)(1-\cos\theta) + \frac{1}{4}\arccos\frac{1}{1+\left(w_1^2/l^2\right)}. \tag{11}$$

When the plastic strain of one point in the plastic hinge line reaches its limiting value, the plate stops cracking and the crevasse size reaches a maximum:

$$y = \frac{l(1-\cos\theta)}{1+\varepsilon_f - \cos\theta - (1/4)\arccos\left(1+\left(w_1^2/l^2\right)\right)^{-1}}, \qquad \theta = \arctan\frac{w_1}{l}. \tag{12}$$

3.1. Crevasse Size of the Plate at Motion Mode I. Under the applied load of $p_0 < p_m < p_{mb1}$, p_{mb1} is the load when the velocity of the plate is zero, $p_{mb1} = 2p_0 - (p_0 t_0/t_s)$ [20], the plate is at motion mode I. Thus, its motion is restricted to only one phase, that is, the impact load and inertial force are responsible for the plate motion. The plate will stop moving when these loads become zero.

According to [20], the final residual deflection of the plate centre can be calculated as follows:

$$w_1^*(t_d) = \frac{p_0 t_s (t_m - t_0)^3}{3\rho_0 t_0 t_m^2}\left[2t_s - t_m + 2\sqrt{t_s(t_s - t_m)}\right], \tag{13}$$

where t_d is the time at the end of the plate movement, t_s is the explosion load duration, t_m is the time when the load reaches the peak pressure, and t_0 refers to the time when plate moves as a pentahedron, which can be defined by $t_0 = p_0 t_m / p_m$.

By substituting (13) into (12), the crevasse size at motion mode I can be obtained as (14).

3.2. Crevasse Size of the Plate at Motion Mode II. Under the explosion load of $p_{mb1} < p_m \le 2p_0$, the plate motion at motion mode II has two phases. The first phase is when the plate moves under the impact load and inertial force from time t_0 to t_s. The second phase is when the plate moves under the inertia force from the time t_s to t_d and stops moving at t_d.

The deflection at the end of the first phase satisfies the idea of the plate at motion mode I and can be obtained according to (10) as (15).

Then, the crevasse size of the plate can be calculated as (16).

When $t = t_s$, the impact load value becomes zero. After that, the plate continues to move under an inertial force and crevasse continues to expand until the motion ends at (17).

The final residual deflection of the plate at motion mode II can be calculated as (18).

Finally, the maximum crevasse size can be determined as (19)

$$y = \frac{l(1-\cos\theta)}{1+\varepsilon_f - \cos\theta - (1/4)\arccos\left(l^2/\left(l^2 + \left\{\left(\left(p_0 t_s (t_m - t_0)^3\right)/\left(3\rho_0 t_0 t_m^2\right)\right)\left[2t_s - t_m + 2\sqrt{t_s(t_s - t_m)}\right]\right\}^2\right)\right)}, \qquad \theta = \arctan\frac{p_0 t_s (t_m - t_0)^3\left[2t_s - t_m + 2\sqrt{t_s(t_s - t_m)}\right]}{3\rho_0 t_0 t_m^2 l}, \tag{14}$$

$$y = w_1(t_s) = \frac{p_0}{3t_0}\left(2t_m t_s^2 - 3t_0 t_s^2 - t_s t_m^2 + 3t_0^2 t_f - t_0^3\right), \tag{15}$$

$$y = \frac{l(1-\cos\theta)}{1+\varepsilon_f - \cos\theta_1 - (1/4)\arccos\left(l^2/\left(l^2 + \left[\left(p_0/3t_0\right)\left(2t_m t_s^2 - 3t_0 t_s^2 - t_s t_m^2 + 3t_0^2 t_f - t_0^3\right)\right]^2\right)\right)}, \qquad \theta = \arctan\frac{p_0\left(2t_m t_s^2 - 3t_0 t_s^2 - t_s t_m^2 + 3t_0^2 t_f - t_0^3\right)}{3t_0 l}, \tag{16}$$

$$t_d = \frac{t_m t_s + t_0^2}{2t_0}, \tag{17}$$

$$w_2(t_d) = \frac{p_0}{12\rho_0 t_0^2}\left(6t_0^2 t_m t_s - 4t_0 t_m^2 t_s + 3t_m^2 t_s^2 - 4t_0 t_m t_s^2 - t_0^4\right), \tag{18}$$

$$y = \frac{l(1-\cos\theta_1)}{1+\varepsilon_f - \cos\theta_1 - (1/4)\arccos\left(\left(12\rho_0 t_0^2 l\right)^2 / \left(\left(12\rho_0 t_0^2 l\right)^2 + \left[p_0\left(6t_0^2 t_m t_s - 4t_0 t_m^2 t_s + 3t_m^2 t_s^2 - 4t_0 t_m t_s^2 - t_0^4\right)\right]^2\right)\right)},$$
$$\theta = \arctan\frac{p_0\left(6t_0^2 t_m t_s - 4t_0 t_m^2 t_s + 3t_m^2 t_s^2 - 4t_0 t_m t_s^2 - t_0^4\right)}{12\rho_0 t_0^2 l}. \tag{19}$$

4. Plastic Deformation and Crevasse Size of a Square Plate under a High Load

Let $p(t_b) = p_b$ and $p(t_m) = p_m$, then $t_m > t_b$ when $p_m > p_b$. When $t_0 < t \le t_b$, the explosion load is the medium load, and the plastic zone and crevasse size can be obtained using the relevant functions presented in the previous chapter. When $t > t_b$, a plastic platform that changes with the applied load appears in the plate, which results in two different plastic zones, as shown in Figure 7. Zone I is the plastic platform expressed for $0 \le z \le \varphi$, where φ is a straight line paralleled to PQ to define the limits of zone I. Zone II is a rigid deformation zone divided by the diagonal plastic hinges and can be expressed for $\varphi \le z \le 1$.

4.1. Plastic Zone of the Plate under a High Load. The plastic zone of the plate is determined when the moving hinge line reaches its limited state. It is assumed that the position of the moving hinge line is φ_c at the time t_c.

The plastic state of zone I is defined as follows:

$$\begin{aligned} M_{xy} &= 0, \\ M_x = M_y &= M_s, \\ v(x,\ y,\ t) &= v(t). \end{aligned} \tag{20}$$

The plastic state of zone II is defined as follows:

$$\begin{aligned} M_x &= M_s + x^2 f(z,\ t), \\ M_y &= M_s + y^2 f(z,\ t), \\ M_{xy} &= xy f(z,\ t), \\ v(x,\ y,\ t) &= v(t)\frac{1-z}{1-\varphi}, \quad \varphi \le z \le 1, \end{aligned} \tag{21}$$

where $f(z,\ t) \le 0$.

Apparently, the boundary condition and speed continuity condition are both satisfied by the velocity field in the above functions. In addition, the plastic hinge line is plastic since $\partial v/\partial\alpha$ is discontinuous at $z = \varphi$.

Substituting $t = t_b = 2t_0$ into (10) and its first derivative, the initial velocity and initial displacement conditions of the plate movement under a high load can be obtained:

$$v_1(x, y, t_b) = \frac{p_0 t_0}{\rho_0}(1-z), \tag{22}$$

$$w_1(x, y, t_b) = \frac{p_0 t_0^2}{3\rho_0}(1-z). \tag{23}$$

Considering the initial force, the equations of motion of the plate can be calculated as follows:

$$\begin{aligned} \frac{\partial Q_x}{\partial x} + \frac{\partial Q_y}{\partial y} &= -p + \rho_0 \ddot{w}, \\ Q_x &= \frac{\partial M_x}{\partial x} + \frac{\partial M_{xy}}{\partial y}, \\ Q_y &= \frac{\partial M_y}{\partial y} + \frac{\partial M_{xy}}{\partial x}. \end{aligned} \tag{24}$$

Substituting (20) and the initial conditions in (22) and (23) into the above equations of motion, the velocity and displacement of zone I can be calculated as follows:

$$\rho_0 v(t) = p_0 t_0 + \int_{t_b}^{t} p(\tau)\, d\tau, \tag{25}$$

$$\rho_0 w(t) = p_0 t_0 t - \frac{5}{3}p_0 t_0^2 + \int_{t_b}^{t} (t-\tau)p(\tau)\, d\tau. \tag{26}$$

Similarly, substituting (21) into (24), the differential equation of $f(z,\ t)$ can be obtained as (27).

Hence, the general solution of $f(z,\ t)$ is expressed as (28):

$$\begin{aligned} z^2 f'' + 6zf' + 6f &= -p(t) \\ &\quad + \rho_0(1-z)\frac{\dot{v}(t)[1-\varphi(t)] + v(t)\dot{\varphi}(t)}{[1-\varphi(t)]^2}, \\ A &= \frac{\partial[v(t)/(1-\varphi(t))]}{\partial t} \\ &= \frac{\dot{v}(t)[1-\varphi(t)] + v(t)\dot{\varphi}(t)}{[1-\varphi(t)]^2}, \end{aligned} \tag{27}$$

$$f(z,\ t) = -\frac{p}{6} + \frac{\rho_0 A}{12}(2-z) + C_3 z^{-2} + C_4 z^{-3}. \tag{28}$$

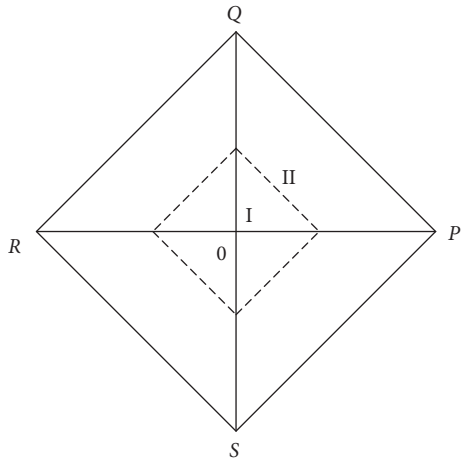

Figure 7: Two different plastic format areas of the plate.

The integration constants C_3 and C_4 can be calculated according to the initial force continuity of the plastic hinge line $z = \theta(t)$:

$$C_3 = -\frac{\rho_0 A - p}{2}\varphi^2 + \frac{\rho_0 A \varphi^3}{3},$$
$$C_4 = \frac{\rho_0 A - p}{3}\varphi^3 - \frac{\rho_0 A \varphi^4}{4}. \tag{29}$$

Considering the clamped boundary condition $M_\alpha(z)|_{z=1} = -M_s$,

$$f(z) l^2 z^2\big|_{z=1} = -2M_s. \tag{30}$$

Substituting the analytic expression of $f(z)$ into the above equations,

$$(\varphi - 1)^2 \left[p(2\varphi + 1) + \frac{\rho_0 A}{2}(3\varphi + 1)(\varphi - 1) \right] = p_0. \tag{31}$$

Here, substituting (25) into the expression of A,

$$p(1-\varphi)^2(\varphi+1) - \left[p_0 t_0 + \int_{t_b}^{t} p(\tau)\, d\tau \right](3\varphi+1)(1-\varphi)\dot{\varphi} = 2p_0. \tag{32}$$

Consequently, combining (1) and (25) into (32), the expression for $\varphi = \varphi(t)$ can be obtained to determine the size of the plastic zone.

The expression of $\varphi(t)$ should be calculated based on different stages since the explosion load is simplified into the triangular load with an ascent stage.

First, considering the ascent stage at $0 \le t \le t_m$,

$$\int_{t_b}^{t} p(\tau)\, d\tau = \int_{t_b}^{t} \frac{p_m}{t_m}\tau\, d\tau = \frac{p_0}{2t_0}\left(t^2 - 4t_0^2\right). \tag{33}$$

Substituting (33) into (32), we get the following:

$$2(1-\varphi)^2(1+\varphi)t - \left(t^2 - 2t_0^2\right)(3\varphi+1)(1-\varphi)\dot{\varphi} = 4t_0. \tag{34}$$

The initial condition of the above equation is $\varphi(t)|_{t=2t_0} = 0$, and the solutions of (33) that satisfy $0 \le \varphi(t) \le 1$ can be calculated with the assistance of the Maple software package.

The moving law of the plastic hinge line at the ascent stage of the simplified explosion load is obtained. The first-order derivative is equal to the first function in (35), which represents the moving velocity of the moving hinge. Furthermore, the plastic zone can be determined if we assign a value of zero to the velocity of the moving hinge line. However, the velocity of the moving hinge has not reached zero at $t = t_m$. Thus, it is necessary to discuss the following:

$$\varphi(t) = \frac{1}{3} - \frac{\xi_1^{1/3}}{6} - \frac{2}{3\xi_1^{1/3}} - \sqrt{3}\left(\frac{\xi_1^{1/3}}{12} - \frac{2}{3\xi_1^{1/3}}\right)i,$$
$$\xi_1 = \frac{\left[-8t^2 - 65t_0^2 + 54t_0 t + 3\sqrt{3t_0\left(156t^2 t_0 + 147t_0^3 - 32t^3 - 260t_0 t\right)}\right]}{\left(t^2 - 2t_0^2\right)}, \tag{35}$$

$$\int_{t_b}^{t} p(\tau)\, d\tau = \int_{t_b}^{t_m} \frac{p_m}{t_m}\tau\, d\tau + \int_{t_m}^{t} \frac{p_m}{t_m - t_s}(\tau - t_s)\, d\tau = \frac{p_0}{2t_0}\,\frac{t_m^2 t_s - 4t_0^2 t_m + 4t_0^2 t_s + t_m t^2 - 2t_s t_m t}{t_m - t_s}, \tag{36}$$

$$\left[\left(t_m^2 t_s - 2t_0^2 t_m + 2t_0^2 t_s\right) + t_m\left(t^2 - 2t_s t\right)\right](3\varphi+1)(1-\varphi)\dot{\varphi} - 2t_m(t - t_s)(1-\varphi)^2(1+\varphi) = 4t_0(t_s - t_m), \tag{37}$$

$$\varphi(t) = \frac{1}{3} - \frac{\xi_2^{1/3}}{12} - \frac{4}{3\xi_2^{1/3}} - \sqrt{3}\left(\frac{\xi_2^{1/3}}{12} - \frac{4}{3\xi_2^{1/3}}\right)i,$$

$$\begin{aligned}\xi_2 = \Bigg(4\Big\{&27\left(1-\varphi_m-\varphi_m^2+\varphi_m^3\right)\left(t_m^3-t_m^2t_s-2t_mt_0^2+2t_st_0^2\right)+4\left(27t_mt_0+8t_mt_s-27t_0t_s\right)t+4t_0\left(t_m-t_s\right)\left(8t_0-27t_m\right)-16t_mt^2\\&-16t_m^2t_s+3\sqrt{3}\Big\{\left(t_m-t_s\right)\left[4t_0\left(t-t_m\right)+\left(t_m^2-2t_0^2\right)\left(1-\varphi_m-\varphi_m^2+\varphi_m^3\right)\right]\left[-32t_mt^2+4\left(27t_mt_0+16t_mt_s-27t_0t_s\right)t\right.\\&\left.+27\left(1-\varphi_m-\varphi_m^2+\varphi_m^3\right)\left(t_m^3-t_m^2t_s-2t_mt_0^2+2t_st_0^2\right)+4t_0\left(t_m-t_s\right)\left(16t_0-27t_m\right)-32t_m^2t_s\right]\Big\}^{1/2}\Big\}\Bigg)\\&\cdot\left(\left(t_mt^2-2t_mt_0^2+t_m^2t_s+2t_st_0^2-2t_mt_st\right)^2\right)^{-1},\end{aligned} \tag{38}$$

The condition of $t \geq t_m$ since the plastic deformation at this time has not reached its maximum value.

When $t = t_m$, (36) can be obtained.

Substituting the above equations into (31) leads to (37). The solutions of (37) that satisfy $0 \leq \varphi(t) \leq 1$ can be obtained as (38).

The moving law of the plastic hinge line during the entire applied explosion load progress has been determined. To investigate the maximum plastic zone, the time required for the plastic hinge line velocity to become zero should be determined. Then, substituting the time value into (31), we get the following:

$$\dot{\varphi} = \frac{p(1-\varphi)^2(1+\varphi) - 2p_0}{\rho_0 v(t)(1+3\varphi)(1-\varphi)}. \tag{39}$$

Since $\dot{\varphi} = 0$,

$$p(1-\varphi)^2(1+\varphi) - 2p_0 = 0. \tag{40}$$

The time when the moving hinge line velocity becomes zero can be calculated by substituting the second expression of the simplified explosion load and (38) into (40):

$$t_c = \frac{3t_0}{2} + \frac{1}{2}\sqrt{4t_mt_s - 12t_0t_s + t_0^2 + \frac{8t_st_0^2}{t_m}}. \tag{41}$$

The plastic zone can be determined as (42) by substituting (41) into (38):

4.2. Crevasse Size of the Square Plate under a High Load. Under a high load of $p_m > p_b$, there are two different motion zones in the plate. The plate is at a plastic state in zone I and the central plate is damaged when the vertical displacement reaches a certain value. As the vertical displacement increases, the cracks continue to propagate along the diagonal line of the plate forming four rigid moving pieces. The motion energy of each piece transforms into bending energy to rotate around the plastic hinge line and fracture energy for the crack expansion. The crevasse size reaches its maximum value when the plastic hinge line expands to its maximum.

The four fractured pieces [21] are shown in Figure 8. The angle of AOB is $\pi/2$, and OA represents the crack length. AB

$$\varphi(t_c) = \frac{1}{3} - \frac{\xi_2^{1/3}}{12} - \frac{4}{3\xi_2^{1/3}} - \sqrt{3}\left(\frac{\xi_2^{1/3}}{12} - \frac{4}{3\xi_2^{1/3}}\right)i,$$

$$\begin{aligned}\xi_2 = \Bigg(4\Big\{&27\left(1-\varphi_m-\varphi_m^2+\varphi_m^3\right)\left(t_m^3-t_m^2t_s-2t_mt_0^2+2t_st_0^2\right)+4\left(27t_mt_0+8t_mt_s-27t_0t_s\right)t_c+4t_0\left(t_m-t_s\right)\left(8t_0-27t_m\right)\\&-16t_mt_c^2-16t_m^2t_s+3\sqrt{3}\Big\{\left(t_m-t_s\right)\left[4t_0\left(t_c-t_m\right)+\left(t_m^2-2t_0^2\right)\left(1-\varphi_m-\varphi_m^2+\varphi_m^3\right)\right]\left[-32t_mt_c^2+4\left(27t_mt_0+16t_mt_s-27t_0t_s\right)t_c\right.\\&\left.+27\left(1-\varphi_m-\varphi_m^2+\varphi_m^3\right)\left(t_m^3-t_m^2t_s-2t_mt_0^2+2t_st_0^2\right)+4t_0\left(t_m-t_s\right)\left(16t_0-27t_m\right)-32t_m^2t_s\right]\Big\}^{1/2}\Big\}\Bigg)\\&\cdot\left(\left(t_mt^2-2t_mt_0^2+t_m^2t_s+2t_st_0^2-2t_mt_st\right)^2\right)^{-1},\\t_c = \frac{3t_0}{2} + \frac{1}{2}&\sqrt{4t_mt_s-12t_0t_s+t_0^2+\frac{8t_st_0^2}{t_m}}.\end{aligned} \tag{42}$$

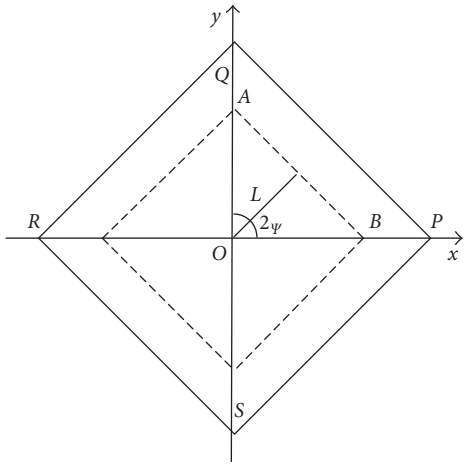

Figure 8: Petal-like cracking of the plate.

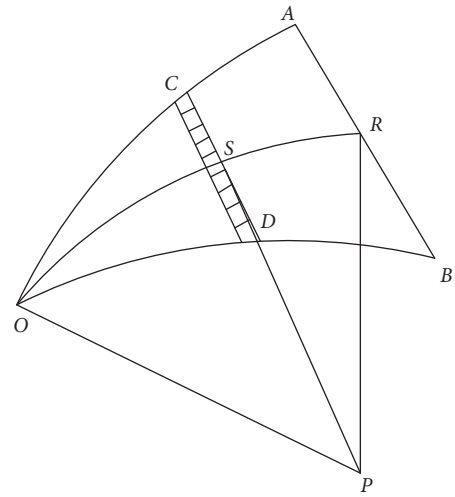

Figure 9: Warped triangular lobes.

refers to the plastic hinge line at the root of the fractured pieces, which moves towards the boundary when the crack OA expands along the y-axis. The moving velocity of AB can be expressed as $\dot{L}$, and L shows the triangle height of AB. At this moment, the triangular piece OAB warps, as shown in Figure 9. The curve OR represents the deformation of piece OAB and can be regarded as an arc with a circular centre at P and radius R. The moving velocity of the plate in zone I can be calculated with (27). Therefore, the energy of motion of the piece OAB can be expressed as follows:

$$E_k = \int_0^L \frac{1}{2} v^2 \, dm = \int_0^L \frac{1}{2} v^2 \cdot \rho_0 \cdot 2h \cdot 2L \cdot dl = \rho_0 h L^2 v^2, \tag{43}$$

$$E_b = M_s l_{\mathrm{AB}} \phi_2, \tag{44}$$

where l_{AB} is the length of AB and ϕ_2 represents the rotating angle of AB.

The variation ratio of the bending energy with time can be calculated as follows:

$$\dot{E}_b = M_s l_{\mathrm{AB}} \dot{f}_2 = 2M_s \frac{\dot{L}}{R} L \tan \psi. \tag{45}$$

Here, R refers to the radius of the piece and can be expressed as $R = 0.8L^{0.6}h^{0.4}$ and ψ is the angle of the triangular piece with $\psi = \pi/4$.

The variation ratio of the fracture energy of the plate can be calculated as [8]:

$$\dot{E}_m = 3.84 M_s h^{-1} \delta_h^{1/3} R^{2/3} \dot{Y} (\sin \psi)^{-(4/3)} (\cos \psi)^{-1}, \tag{46}$$

where δ_h has the value of 1 and Y refers to the length of the boundary to the side of the crevasse, which is in a direct line with L.

The plate in zone I is in a plastic state under a high load. The energy of motion of each fracture piece will transform into both bending energy and fracture energy:

$$E_k = \int_{t_s}^{t_f} \left(\dot{E}_b + \dot{E}_m \right) dt, \tag{47}$$

where t_s refers to the moment when the moving hinge line at the root of the fracture piece begins to move ($t_s = 2t_0$ under a high load) and t_f is the moment when the hinge line stops moving ($t_f = t_c$).

Consequently, the crevasse size can be obtained as follows:

$$y = \frac{Y}{\cos \psi} = \sqrt{2} Y. \tag{48}$$

4.3. Crevasse Size of the Plate at Motion Mode III. Under the explosion load of $2p_0 < p_m < p_{mb2}$, where $p_{mb2} = 4p_0 - 4p_0 t_0 / t_s$, the plate is at motion mode III. When the applied explosion load becomes zero at $t = t_s$, the velocity of the plate in zone I can be expressed as follows:

$$v(t_s) = \frac{p_0}{\rho_0 t_0} \left(t_s t_m - 2t_0 t_s + t_0^2 \right). \tag{49}$$

Geometrically,

$$L = \frac{l}{2} Z = \frac{l}{2} \varphi(t). \tag{50}$$

When the applied load is over, the motion energy of each fracture piece can be obtained:

$$E_k = \frac{h p_0^2 l^2}{4 \rho_0 t_0^2} \left(t_s t_m - 2t_0 t_s + t_0^2 \right)^2 \varphi^2 (t_s). \tag{51}$$

Substituting (50) into (45) and combing the values of ψ and R, the equation of the variation ratio of the bending energy can be simplified as follows:

$$\dot{E}_b = \frac{3.77 M_s \dot{\varphi}(t)}{l^{0.6} h^{0.4} \varphi^{1.6}(t)}. \tag{52}$$

Similarly, the equation of the variation ratio of the fracture energy can be simplified as follows:

$$\dot{E}_m = 5.65 M_s l^{0.2} h^{-(2.2/3)} \dot{Y}. \tag{53}$$

The crevasse size of the plate at motion mode III can be obtained:

$$y = \sqrt{2}Y,$$

$$Y = \frac{\left(\left(hp_0^2l^2\right)/\left(4\rho_0t_0^2\right)\right)\left(t_st_m - 2t_0t_s + t_0^2\right)^2\varphi^2\left(t_s\right) - \left(\left(3.77M_s\right)/\left(l^{0.6}h^{0.4}\right)\right)\int_{2t_0}^{t_c}\left(\dot{\varphi}\left(t\right)/\varphi^{1.6}\left(t\right)\right)dt}{5.65M_sl^{0.2}h^{-(2.2/3)}\left(t_c - 2t_0\right)}. \tag{54}$$

4.4. Crevasse Size of the Plate at Motion Mode IV. Under the explosion load of $p_m > p_{mb2}$, the plate is at motion mode IV. The difference in calculating the crevasse size for modes III and IV is the different moving velocity when the applied load becomes zero, which results in different motion energy.

When the explosion load becomes zero at $t = t_s$, the velocity of the plate in zone I can be calculated as follows [11]:

$$v\left(t_s\right) = \frac{p_0}{2\rho_0t_0}\left(t_mt_s - 2t_0^2\right). \tag{55}$$

Combing (43), (49), and (55) and $t = t_s$, the motion energy of each fracture piece at the end of the explosion load can be calculated as follows:

$$E_k = \frac{hp_0^2l^2}{16\rho_0t_0^2}\left(t_st_m - 2t_0^2\right)^2\varphi^2\left(t_s\right). \tag{56}$$

Substituting (52), (53), and (56) with $t_s = 2t_0$ and $t_f = t_c$ into (48), the crevasse size of the plate at motion mode IV can be obtained:

$$y = \sqrt{2}Y,$$

$$Y = \frac{\left(\left(hp_0^2l^2\right)/\left(16\rho_0t_0^2\right)\right)\left(t_st_m - 2t_0^2\right)^2\varphi^2\left(t_s\right) - \left(\left(3.77M_s\right)/\left(l^{0.6}h^{0.4}\right)\right)\int_{2t_0}^{t_c}\left(\dot{\varphi}\left(t\right)/\varphi^{1.6}\left(t\right)\right)\,dt}{5.65M_sl^{0.2}h^{-(2.2/3)}\left(t_c - 2t_0\right)}. \tag{57}$$

5. Comparative Analysis

5.1. Comparison Results between Experiment and Theoretical Analysis. To verify the theoretical analysis of the plastic zone of a clamped square plate, the experimental results from the literature are considered [22]. The comparison results are listed in Table 1.

In the experiment, the slit scanning method of optical measurement technology was used to photograph the deformation process of whole test plate. The size of the experimental plates is shown in Table 1 and experimental installation is shown in Figure 10. A symmetrical set of coordinates is drawn on the symmetry line of the test plate to make an angle between the plate and the horizontal plane.

When the plate is deformed, the trajectories of the coordinate points varying with the deformation of the test plate are captured by a high-speed camera, by which the displacement and velocity fields of the test plate can be obtained.

As shown in Table 1, when the plastic hinge line moves to the plate centre, the plastic platform size from the theoretical results is relatively larger than that of the experimental results; however, the errors are quite small when the plastic hinge is located away from the plate centre. Overall, the theoretical results in this paper and the experimental results are nearly identical.

5.2. Material Model. LS-DYNA software is a general purpose nonlinear dynamic analysis finite element programme, which is mainly explicit and supplemented by implicit; it is especially suitable for coping with nonlinear dynamic impact problems such as high-speed collisions, explosion, and metal forming of various 2D and 3D nonlinear structures. Meanwhile, heat transfer, fluid, and fluid-solid coupling problems also exist. Therefore, 8 groups of numerical simulation analyses were carried out by ANSYS/LS-DYNA to compare the results.

In the simulation, the explosive was a spherical TNT charge, and the plate was made of low-carbon steel with four clamped sides. The air was assumed to be an ideal gas with the size of 60 cm × 60 cm × 0.3 cm. Considering the symmetry of the question, a quarter of the plate and air model was created.

The explosive, air, and steel plates were all simulated with unit SOLID164. The model HIGH_EXPLOSIVE_BURN and the JWL equation of state were employed for the explosive:

$$P = A\left(1 - \frac{\omega}{R_1V}\right)e^{-R_1V} + B\left(1 - \frac{\omega}{R_2V}\right)e^{-R_2V} + \frac{\omega E_0}{V}, \tag{58}$$

where p is the explosion pressure; A, B, R_1, R_2, and ω are the material constants relating to the type of explosive; V is the relative volume; and E_0 is the internal energy per unit volume.

The LINEAR_POLYNOMIAL model was employed for the air:

$$P = C_0 + C_1\mu + C_2\mu^2 + C_3\mu^3 + \left(C_4 + C_5\mu + C_6\mu^2\right)E_0. \tag{59}$$

For ideal air, γ is the ideal gas isentropic adiabatic exponent, ρ is the density of the air, and E_0 is the internal energy per unit volume.

Table 1: Comparisons of theoretical and experimental results.

Time (ms)	Plate	σ_s (MPa)	Plate thickness (mm)	Distance from plastic platform edge to the plate centre		
				Experimental (mm)	Theoretical (mm)	Relative error (%)
0.78	Steel	190	1.5	65	67	3.08
	Aluminum 1	85	1.0	54	50	7.41
	Aluminum 2	320	2.0	69	65	5.80
1.54	Steel	190	1.5	15	17	13.33
	Aluminum 1	85	1.0	6	5	16.67
	Aluminum 2	320	2.0	17	20	17.6
2.11	Steel	190	1.5	58	54	6.9
	Aluminum 1	85	1.0	65	69	6.1
	Aluminum 2	320	2.0	46	42	8.7
2.47	Steel	190	1.5	67	71	6.0
	Aluminum 1	85	1.0	73	69	5.5
	Aluminum 2	320	2.0	61	67	8.9

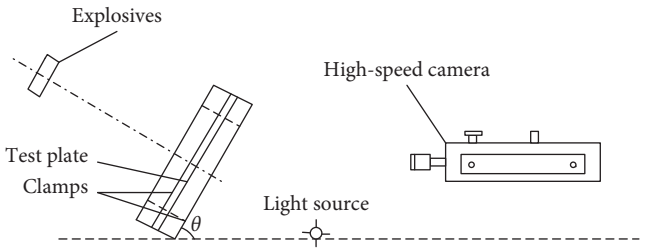

Figure 10: Experimental installation.

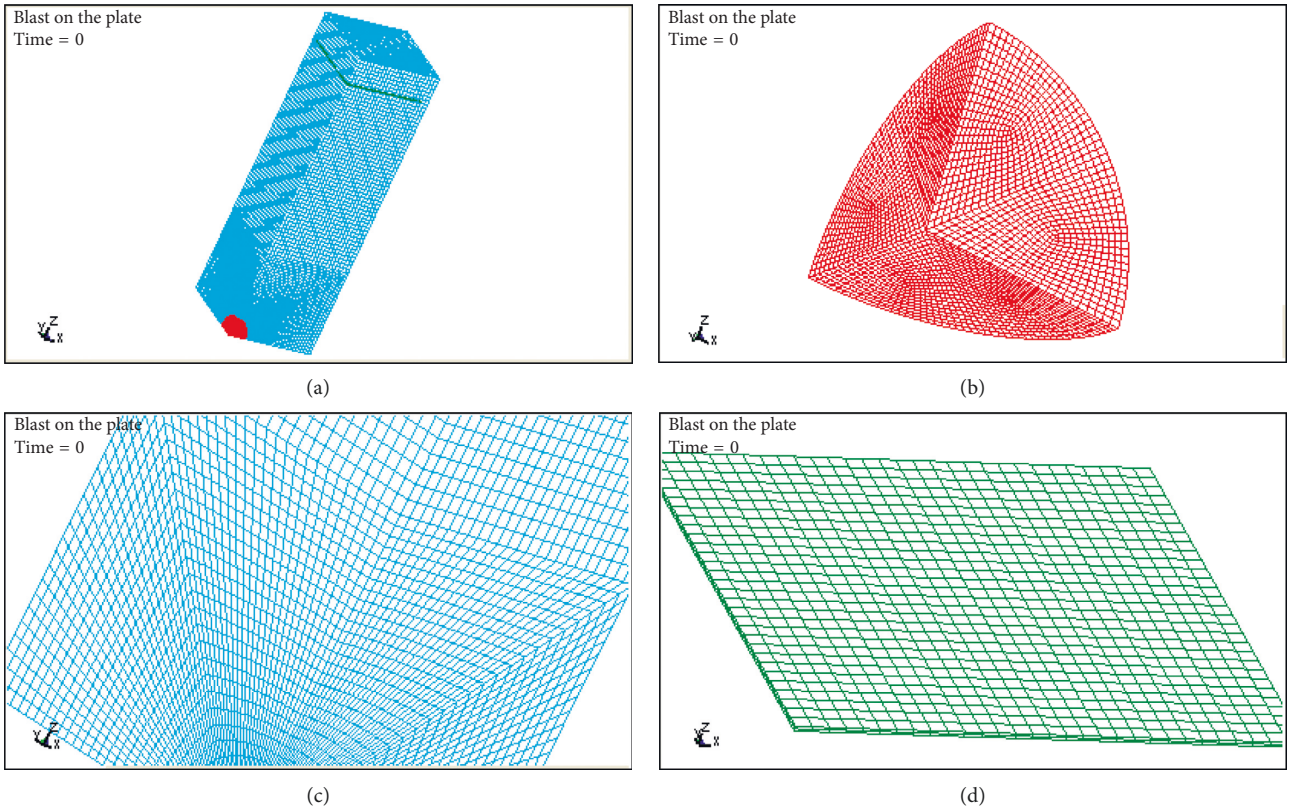

Figure 11: Finite element model.

Table 2: Sensitivity of mesh size on the fracture of plate.

Element size (cm)	1.5	2.0	2.5	3.0
Theoretical value of fracture (cm)	16.5	16.5	16.5	16.5
Simulative value of fracture (cm)	13.4	13.4	12.4	11.3
Relative error (%)	18.7	18.7	24.8	31.5

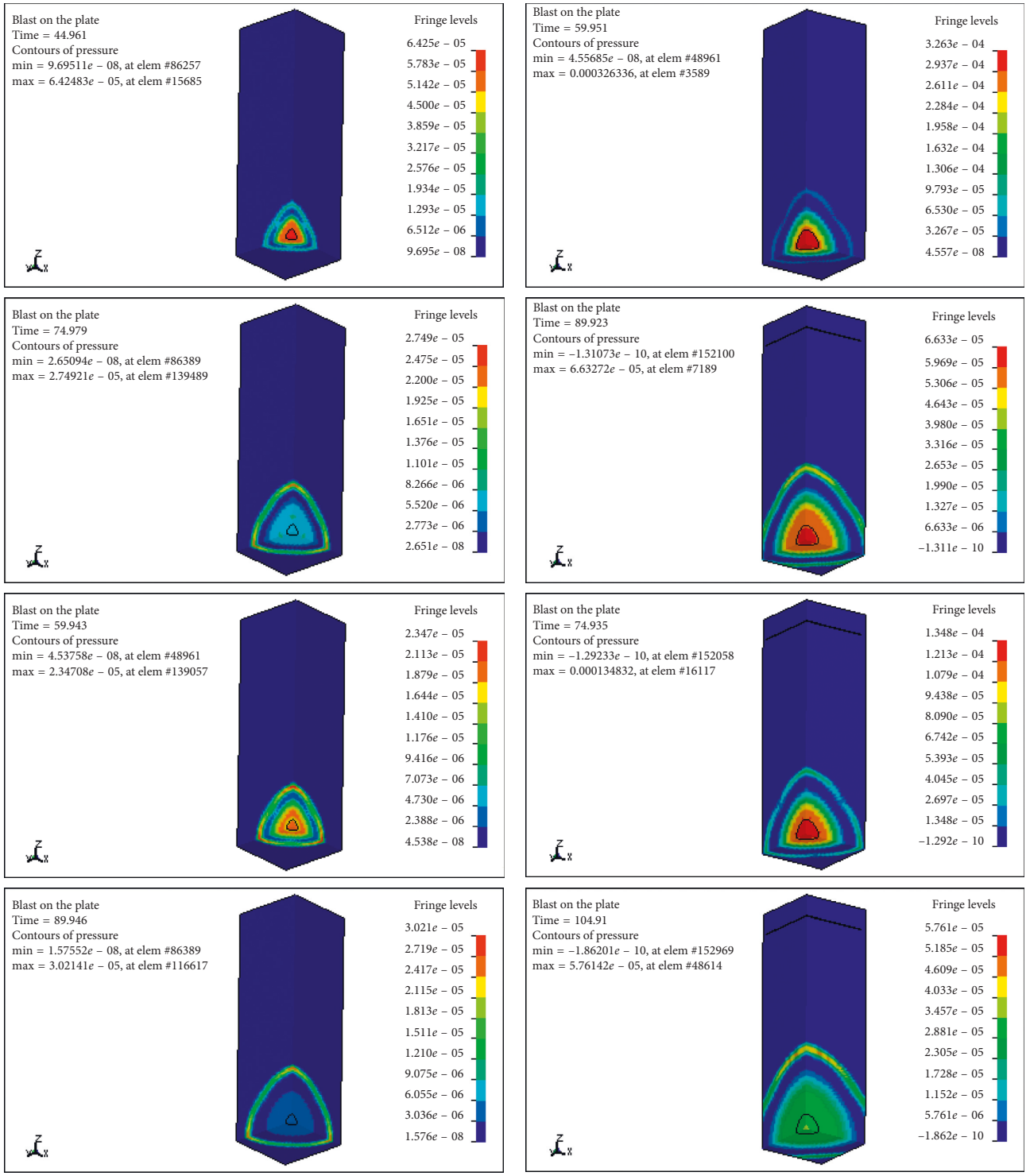

(a) (b)

Figure 12: Waveform of a spherical charge explosion. Explosion waveform of the (a) working condition 1 and (b) working condition 2.

Table 3: Comparisons of theoretical and numerical simulation results.

Samples	Charge radius (cm)	Peak overpressure (kPa)	Motion mode	Theoretical value (mm)	Simulation value (mm)
1-1	2.0	105.7	I	16.5	13.4
1-2	2.5	151.9	I	18.9	15.7
2-1	2.0	105.7	II	21.8	18.3
2-2	2.5	151.9	II	24.1	20.6
3-1	5.0	915.4	III	37.2	35.5
3-2	6.0	1164.3	III	44.1	42.7
4-1	5.0	915.4	IV	48.8	45.2
4-2	6.0	1164.3	IV	53.7	50.2

Steel plates are typically made of ordinary low-carbon steel; because the explosive impact load reaches great pressure in a very short period of time, the influence of strain rate and reinforcement of structural materials must be considered. The nonlinear plasticity model PLASTIC KINEMATIC model material is adopted for consideration of the strain rate effect. The material model is based on the relation of Cowper–Symonds:

$$\sigma_y = \left[1 + \left(\frac{\dot{\varepsilon}}{C}\right)^{1/\mathrm{P}}\right]\left(\sigma_0 + \beta E_{\mathrm{p}} \varepsilon_{\mathrm{eff}}^{p}\right), \tag{60}$$

where σ_0 is the initial yield strength, C and P are the material constants, and β is the enhancement parameter, which varies from 0 to 1. When $\beta = 0$, the model is the plastic follow-up strengthening model; when $\beta = 1$, the model is the isotropic reinforcement model, and E_{p} is the plastic reinforcement modulus; E is the modulus of elasticity and E_{t} is the tangent modulus.

5.3. Meshing of the Model. After the establishment of the geometric model, the next step is to mesh the geometric model. The problems studied in this paper have the characteristics of high speed and large deformation, so high-quality grids are required. Therefore, when meshing, the body is first cut to ensure the satisfaction of the mapping grid conditions. The mapping grid is then used to divide the cells into hexahedrons. The finite element model after meshing is shown in Figure 11.

The size of the air grid around the explosives is smaller during the meshing process because of the drastic changes in the explosives and air. The steel plate also uses a fine meshing size due to the effect of the explosion shock wave. To acquire the appropriate grid size, the sensitivity of the mesh size was studied for a plate with a 2.0 cm charge radius and 0.054 kg dynamite, and the influence of grid size on the size precision of the fracture is shown in Table 2.

According to the relative error of the four experiments, when the mesh size is 1.5 cm and 2.0 cm, the simulation value is closer to the theoretical value. In addition, considering that too fine a mesh will result in long computing time, the mesh size of 2.0 cm is finally used and the air grid away from explosives is relatively large. Explosives and air are modelled by common joints, while steel and air are modelled by noncommon joints. The fluid-solid coupling is then defined to apply explosive loads to the steel plate. In addition, unreflected boundary conditions are applied at the air boundary to avoid the propagation law of the air shock wave affected by the reflection of the shock wave at the air boundary. The way to apply the no reflection boundary condition method is to choose the outer surface of the air model and select the nodes on all nodes which is defined as a group; the no reflection boundary condition on the node group is defined.

5.4. Comparison between the Numerical Simulation and Theoretical Analysis. To analyse the characteristics of the spherical charge near the field explosion load and the peak overpressure of blast wave, a numerical simulation of two different loading radii were carried out. The radius of the load on working condition 1 is 3.5 cm and the loading amount is 0.29 kg. The radius of the load on working condition 2 is 7.0 cm and the loading quantity is 2.30 kg.

The propagation process of shock waves generated by explosive explosion in the air is shown in Figure 12. A blast wave caused by a spherical charge exploding in the air is distributed uniformly in space, and it propagates in all directions in the form of spherical waves. It is similar to the propagation in the free air field before it hits the steel plate. This outcome is in line with the basic theory of explosions, which verifies the accuracy of the numerical simulation of explosions in this paper.

According to the theoretical analysis shown in Sections 3 and 4, the explosion load is divided into high load and medium load, and each load has four motion modes. The fracture size of the square plate under each motion mode has been studied theoretically to verify the correctness of the theoretical analysis, and this section presents eight groups of numerical simulation analyses for every motion mode. The comparison results of the theoretical analysis and numerical simulations are listed in Table 3. As shown in Table 3, the theoretical results are generally larger than the numerical simulation results, mainly because of the ignored strengthening effects of the materials and the effects of the surface force in the theoretical analysis. On the contrary, the results from the numerical study, which took these effects into account, were more accurate than those from the experiment. However, the theoretical analysis in this paper would always be more conservative, so the present approach could provide theoretical guidance for practical engineering.

6. Conclusions

In summary, the plastic zones and crevasse sizes of the plate under medium and high loads were discussed based on the ultimate plastic strain criteria. The following conclusions can be drawn from the analysis.

Under medium load, the plastic zone consisted of the four sides and two diagonals of the square plate. Based on the plate motion when the explosive load becomes zero, the motion was divided into two modes. With reference to the plastic response of the clamped square plate and ultimate plastic strain criteria, the crevasse size formulas of the plate at two different motion models were derived.

Under high load, the plastic hinge lines and the corresponding movement law were discussed, and the plastic zone of the plate was determined. The crevasse sizes of the plate at motion modes III and IV after the explosion load becomes zero were calculated according to the principle of the conservation of energy.

The present theoretical analysis agrees with the experimental and simulation results; this outcome verifies the validity of our approach. This approach is also expected to be extendable to applications in practical engineering.

Data Availability

The data used to support the findings of this study are available from the corresponding author upon request.

Conflicts of Interest

The authors declare that they have no conflicts of interest.

References

[1] L. Wenxian, H. Jijiang, Y. Qiu et al., "Multi-shelled hollow metal-organic frameworks," *Journal of Angewandte Chemie-International Edition*, vol. 56, no. 20, pp. 5512–5516, 2017.

[2] J.-H. Kang, "Vibrations of complex shells with variable thickness," *Journal of Engineering Mechanics*, vol. 143, no. 8, article 04017053, 2017.

[3] P. K. Gupta and R. R. Sahub, "Large deformation studies on combined shell structures," *Procedia Engineering*, vol. 173, pp. 1700–1707, 2017.

[4] P. K. Gupta, "A study on analysis of collapse of metallic shells having dome-cone shape," *Procedia Engineering*, vol. 173, pp. 1708–1715, 2017.

[5] S. K. Clubley, "Non-linear long duration blast loading of cylindrical shell structures," *Engineering Structures*, vol. 59, pp. 113–126, 2014.

[6] J. Y. Wu, C. Ji, Y. Long, K. Song, and Q. Liu, "Dynamic responses and damage of cylindrical shells under the combined effects of fragments and shock waves," *Thin-Walled Structures*, vol. 113, pp. 94–103, 2017.

[7] Z. Zhang, L. Sun, X. Yao, and X. Cao, "smoothed particle hydrodynamics simulation of the submarine structure subjected to a contact underwater explosion," *Combustion Explosion and Shock Waves*, vol. 51, no. 4, pp. 502–510, 2015.

[8] S. Yao, D. Zhang, F. Lu, X. Chen, and P. Zhao, "A combined experimental and numerical investigation on the scaling laws for steel box structures subjected to internal blast loading," *International Journal of Impact Engineering*, vol. 102, pp. 36–46, 2016.

[9] Y. Long, H. Zhou, X. Liang et al., "Underwater explosion in centrifuge Part II: dynamic responses of defensive steel plate," *Science China Technological Sciences*, vol. 60, no. 12, pp. 1941–1957, 2017.

[10] S. Chung Kim Yuen, G. Cunliffe, and M. C. du Plessis, "Blast response of cladding sandwich panels with tubular cores," *International Journal of Impact Engineering*, vol. 110, pp. 266–278, 2017.

[11] R. Houlston and C. G. Desrochers, "Nonlinear structural response of ship panels subjected to air blast loading," *Computer and Structures*, vol. 26, no. 1-2, pp. 1–15, 1987.

[12] K. Spranghers, I. Vasilakos, D. Lecompte, H. Sol, and J. Vantomme, "Identification of the plastic behavior of aluminum plates under free air explosions using inverse methods and full-field measurements," *International Journal of Solids and Structures*, vol. 51, no. 1, pp. 210–226, 2014.

[13] D. Breslavsky, O. Morachkovsky, I. Naumov, and O. Ganilova, "Deformation and fracture of square plates under repetitive impact loading," *International Journal of Non-Linear Mechanics*, vol. 98, pp. 180–188, 2018.

[14] C. Zheng, X. S. Kong, W. G. Wu, and F. Liu, "The elastic-plastic dynamic response of stiffened plates under confined blast load," *International Journal of Impact Engineering*, vol. 95, pp. 141–153, 2016.

[15] Y. Li, W. Wu, H. Zhu, Z. Wu, and Z. Du, "The influence of different pre-formed holes on the dynamic response of square plates under air-blast loading," *Engineering Failure Analysis*, vol. 78, pp. 122–133, 2017.

[16] W. Huang, W. Zhang, X. Huang, X. Jiang, Y. Li, and L. Zhang, "Dynamic response of aluminum corrugated sandwich subjected to underwater impulsive loading: experiment and numerical modeling," *International Journal of Impact Engineering*, vol. 109, pp. 78–91, 2017.

[17] Z. Kazanci and Z. Mecitoglu, "Nonlinear dynamic behavior of simply supported laminated composite plates subjected to blast load," *Journal of Sound and Vibration*, vol. 317, no. 3–5, pp. 883–897, 2008.

[18] S. J. Yao, D. Zhang, and F. Y. Lu, "Dimensionless number for dynamic response analysis of box-shaped structures under internal blast loading," *International Journal of Impact Engineering*, vol. 98, pp. 13–18, 2016.

[19] N. Jones, "Plastic failure of ductile beams loaded dynamically," *Journal of Engineering for Industry*, vol. 98, no. 1, pp. 131–136, 1976.

[20] H. Jian, Z. Mingwei, T. Aipeng, and S. Shuxin, "Blast-resistance dynamic analysis of clamped square plates," *Journal of Harbin Engineering University*, vol. 32, pp. 1569–1575, 2011.

[21] Z. H. Zhang and X. Zhu, "Petaling of rigid plastic plate under contact explosive loading of cylindrical dynamite," *Journal of Ship Mechanics*, vol. 8, pp. 113–119, 2004.

[22] X. Zhu, L. Zhu, and M. D. Yin, "Experimental study on plastic deformation process of clamped square plate subjected to explosive loadings," *Journal of Naval University of Engineering*, vol. 2, pp. 61–65, 1985.